

# Low Current Diagnostic Devices for Radioactive Beams

**D. Shapira**

*Physics Division, Oak Ridge National Laboratory, Oak Ridge, Tennessee, USA*

## **Abstract**

This contribution reviews detectors used for low intensity radioactive beam diagnostics. Emphasis is on diagnostic devices that are based on the detection of secondary products (ions, electrons) resulting from the interaction of the beam with a thin detection medium. Devices based on this principle can be tailored to work with low energy ( $< 10 \text{ MeV/A}$ ) ion beams available at current and planned ISOL type RB facilities.

PACS:

Keywords:

Corresponding author:

D. Shapira

Oak Ridge National Laboratory

Bldg, 6000, MS-6368

Oak Ridge, TN 37831-6368, USA

Phone: 865-572-2648

Fax: 865-574-1268

E-Mail: [shapirad@ornl.gov](mailto:shapirad@ornl.gov)

Refence Abstract #99

## **1. Introduction**

Beam diagnostic devices appropriate for radioactive beams (RB) with kinetic energies ranging from a few keV/A to a few MeV/A are listed in Table 1. Of these, some are not specific to low-intensity radioactive beam detection but have been used at low-beam intensities following slight modifications.

Of the methods listed in Table 1 most suited for monitoring low energy ( $<10\text{MeV/A}$ ) and low-intensity radioactive beams are those based on detecting secondary emission from interactions of the passing beam particles. The performance and characteristics of detectors based on this principle as well as perceived shortcomings and proposed remedies will be discussed in the following sections.

## **2. Residual gas beam profile sampling detector**

The principle of operation of this detector is outlined in Fig. 1. The ion and electron formed in collision of residual gas atoms with beam particles are collected at the two electrodes straddling the beam path. The position signal at the cathode and the ion drift time yield the location of the ionizing collision thus yielding a sample of the beam path in three dimensions. Figure 2a displays the raw position signal recorded at the cathode, using the resistive layer to provide position signals in two dimensions. In spite of the noticeable level of background, the beam trajectory is clearly delineated. The vertical drift time spectrum shown in Fig 2b is more complex. The positive-ion drift time depends on the position at which ionization occurred and on the mass of the ion. Since

the residual gas in the evacuated beam pipe is a mixture containing a variety of molecules, the position spectrum may become undecipherable. In order to better determine the ion position, we seeded the device with dry nitrogen. The system was first pumped to a pressure of  $10^{-7}$  Torr and then let up to  $10^{-6}$  Torr nitrogen using a controlled leak. The strongest and narrowest peak in the spectrum is due to  $N_2^+$  drift time and has a width corresponding to  $\sim 1$  cm FWHM. The observed width reflects the beam spread at a position half way between the focusing magnet and the target location.

The data in Fig. 2 were accumulated during a five minute long exposure to a mixture of  $^{17}F/^{17}O$  beams with intensity of  $4 \times 10^5/s$ . It is clear that for beam intensities below  $10^4$ , the background seen in Fig. 2b will become significant. This background at rate of about 0.2/s was found to be independent of beam intensity or ambient gas pressure. In order to obtain position information at beam rates below  $10^4/s$  one would need to lower the background rates or increase the sampling probability by raising the nitrogen partial pressure. Figure 2c shows how the measured sampling probability tracks variation in ambient gas pressure.

This device could also be used in monitoring the driver beam aimed at the production target. For this application the device should be pumped to a very low ambient pressure. At ambient pressures near  $10^{-9}$  Torr, the expected sampling rate for a  $10 \mu A$  proton beam should be near  $10^5/s$ . The advantage of such a beam monitor should be obvious. Once the beam is tuned on to the production target it passes through the device unscathed, yet

the accelerator operator has a continuous reading of the driver beam position and intensity.

### **3. Devices based on secondary electron emission from foils**

Figures 3a and 3b show two geometries of beam diagnostic device based on sensing the beam position by detecting secondary electrons emitted from a thin foil inserted in the beam's path. The two designs shown here are generic. The detectors that detect the electrons and measure their position can, and do, vary. Some devices were constructed where the MCP was used to multiply the electrons and the electrons exiting the back of the MCP were then accelerated on to a phosphor viewed by a digital camera [8]. Other designs use a position-sensitive gas-filled detector to detect the electron [9].

These detectors are well suited for detection of radioactive ion beams. Since electron emission is a surface effect, the foils can be as thin as can be produced [10], and therefore, the beam suffers minimal scattering. The efficiency of electron ejection depends only on the specific ionization of the projectile ( $dE/dx$ ) and for heavy ions with energies in the range of  $0.1\text{MeV/A} < E_{\text{kin}} < 10\text{MeV/A}$ , it is close to 1.0.

These detectors, however, do not have good position resolution. The detectors shown in Fig 3a and Fig 3b have position resolution that is no better than 5% of the electron drift distance (*i.e.*, 2-3 mm). We have shown that the observed spread in position is caused by the velocity distribution of the electron when it is emitted from the foil [11]. The

addition of a magnetic field approximately parallel to the accelerating electrostatic field (an “electron paralleliser”) improves the position resolution that can be obtained with such devices [7]. The configuration of such a detector is shown in Fig. 4 where two permanent magnets provide the required magnetic field. Data taken with two different detector configurations, one with the magnetic field set for optimum resolution (large magnification) and the other with substantial image demagnification are shown in Figs. 5 and 6.

## **4. Examples**

### **4a. Beam counting**

The detectors shown in Fig. 3 also deliver a good timing signal and can be used for beam counting. As shown in Ref. 12, however, these detectors are not guaranteed to deliver 100% detection efficiency under all circumstances. Approximate efficiency of such detectors can be predicted and measured [7, 12], but in order to ensure true counting the efficiency must be monitored during the experiment. The method outlined in Fig. 7 uses two detectors to count beam particles and monitor the counting efficiency continuously. Sample efficiency data taken during a run with 160 MeV  $^{17}\text{F}$  particles are shown in Fig. 8. The beam intensity was near 2-3 MHz and the measured efficiency is about 40% in keeping with predicted values [7].

### **4b. Isobar separation and tagging**

Present day RB facilities deliver beams that often contain mixtures of isobars. At the energy range typical to ISOL facilities separating these isobars is not a not trivial task. Among the methods used to study beam composition are beam essays where the beam is implanted on a stationary thick target for a measured time period and the activity is monitored at several time intervals following the implantation. Implantation on a moving tape that transports radioactive ion deposited to remote counting stations is also used for beam essays. Another sampling technique is based on studying the X-ray excitation of the different isobar in the beam. This is a sampling technique that can be used to study isobaric composition of the beam. Data taken by D. Radford et al. [13], presented in Fig. 9, show test data taken with separate stable beams, as well as the X-ray spectrum obtained from a mixture of  $A = 126$  and  $A = \mathbf{124}$  isobars in radioactive ion beams.

There may be cases where sampling is not sufficient and complete separation or tagging of different isobars in the beam is required. Many contributions to this conference describe such techniques as traps that can be used on cold beams or EM spectrographs used with energetic beams. In some cases, such tagging or separation can be done with the simple technique displayed in Fig. 10, which relies on the well-known dependence of energy loss on the ion's nuclear charge. Note that for the energy regime for beams available from ISOL facilities, the main hindrance to the efficacy of this method is homogeneity of the energy degrading absorber. It is virtually impossible to get the thin solid absorber material (in the  $\text{mg}/\text{cm}^2$  range) with the required homogeneity  $<0.5\%$ . Using a specially designed gas cell [16] and an improved formulation of energy

stragglers, we have demonstrated that one could predict the degree of isobar separation attainable with this method. Figure 11a shows the predicted (simulated) separation attainable for  $A = 132$  isobars with kinetic energies near 450 MeV [16]. Figure 11b shows the measured separation in the test beamline shown in Fig. 10. The isobar separator magnet in the low-energy injection line was retuned leading to changes in the isobaric composition of the accelerated beam (see Fig. 11b). These time-of-flight spectra are accumulated online and can be used to monitor the effect of changes in beam tuning, thus providing immediate feedback to the accelerator operators. There are situations where such separation or beam tagging methods can prove very advantageous. A case in point is presented in Fig. 12 that shows how separated  $^{17}\text{F}$  isobars at 20 MeV can be provided with minimal (<50%) loss in beam intensity. If we were to use stripping to charge state 9+ and subsequent magnetic separation of  $^{17}\text{F}$  from  $^{17}\text{O}$  isobars, we would suffer more than 98% loss in beam intensity at these energies.

### **5c. An electronic phosphor**

For beam tuning the scintillating phosphor screen is a time proven aid, but it typically requires beam intensities higher than  $10^8/\text{s}$ . Use of sensitive CCD cameras and more efficient phosphor can extend usability by 2 to 3 orders of magnitude in beam intensity [1]. For lower beam intensities one can use the output of a position-sensitive detector that counts single particles to emulate the action of a phosphoric screen. An electronic phosphor screen that provides usable beam images with count rates as low as 100 counts/sec is shown in Fig. 13. Hit coordinates on the screen are generated by counts

accumulated in a position-sensitive detector of the type shown in Fig. 4. A circular buffer storing  $X$ - $Y$  hit coordinates is updated and redisplayed a few times per second creating a scintillating dot display with a linear decay time [17].

## 6. Conclusions and outlook

While there are many methods used by scientists to diagnose low-intensity radioactive beams, many lack the maturity attained by methods that have been in use by machine operators. In that vein we have decided to mount one of the beam diagnostics devices depicted in Fig. 3 on a retractable mount that can be operated and sensed remotely and can be energized by applying one or at most two energizing voltages and providing a direct analog readout of count rate and position spectrum. Ostrumov et al. at ANL [15] have built a detector based on these techniques with enhancements that make it a useful tool for measuring beam emittance. We plan further improvements in the performance of this detector type that will concentrate on digital handling of higher count rates, maybe in excess of  $10^7$  particles/sec. This will increase the range of applicability for this type of detector.

Further development of the residual gas beam profile monitor will concentrate on reducing the rate of background counts that at present hovers near 0.2/s. This detector has been operated inside storage rings where large magnetic fields are present and with high-beam intensities [16] showing that it can be used for continuous monitoring of the driver beam's position and intensity on its way to the production target.

## References:

1. R. C. Rogers, D. P. May, V. Horvat, G. Kim, R. Gutierrez – The Texas A&M University Cyclotron Institute Single Event Effect Facility – Preprint and private comm.
2. R. Michaelsen and E. Seidel, *Nucl. Instrum. and Methods* **A268** (1988), 503.
3. M. C. Ross, J. T. Seeman, R. K. Jobe, J. C. Sheppard and R. F. Sterling, Particle Accelerator Conference Vancouver, BC, 1985.
- 4a. P. Finocchiaro, A. Amato., G. Ciavola, G. Cuttone, M. Gu, G. Raia, A. Rovelli, *Nucl. Instrum. and Methods* **A385** (1997), 31.
- 4b. K. Kuroda, F. Lehar, S. Makino, A. Michalowicz, A. Penzo and F. Takeutchi, *Nucl. Instrum. and Methods* **A300** (1991), 259.
5. O. Klepper, C. Kozhuharov, Contribution to this conference EMIS-I4 #46; and K. E. Rehm, M. Paul, J. Gehring, B. Glagola, D. Henderson, W. Kutchera and A. H. Wousmaa, *Nucl. Instrum. and Methods* **A344** (1994), 614.
6. D. Shapira, T.A. Lewis and J. L. Mosher, *Nucl. Instrum. and Methods* **A400** (1997) 185.
7. D. Shapira, T. A. Lewis and L. D. Hulett, *Nucl. Instrum. and Methods* **A454** (2000) 409.
8. K. Kruglov, L. Weissman, P. Van den Bergh, A. Andreyev, M. Huyse, P. Van Duppen, *Nucl. Instrum. and Methods* **A 441** (2000) 595.
9. Herve Savajols – VAMOS contribution to this conference EMIS-14 Abstract #92 and L. Pollaco, CEN Saclay, Private Comm.

10. J. P. Greene, C. J. Lister, P. Reiter, G. E. Thomas and K. L. Unterzuber, *Nucl. Instrum. and Methods* **A459** (2001), 334.
11. D. Shapira, T. A. Lewis and L.D. Hulett and Z. Ciao, *Nucl. Instrum. and Methods*, **A449** (2000)396.
12. Y. Zhang, H. J. Whitlow, T. Winzell, I. F. Bubb, T. Sajavaara, K. Arstila, and J. Keinonen, *Nucl. Instrum. and Methods* **B149** (1999), 477.
13. D. Radford et al., *Phys. Rev. Lett.* (in print) and Private Communications.
14. D. Shapira, T. A. Lewis, P. M. Mueller to appear in *Nucl. Instrum. and Methods* **A**.
15. P. N. Ostrumov, P. Billquist, M. Portillo and W. Q. Chen, *Review of Scientific Instruments* **73** (2002), 56.
16. T. Quinteros, D. R. DeWitt, A. Paal, R. Schuch, *Nucl. Instrum. and Methods* **A378** (1996) 35.
17. W. T. Milner display program DDMAN. HRIBF Data acquisition computer manual.

## List of Figures

Fig. 1. The ions transported from the position where ionization of the residual gas molecule occurred retain information on the position of the ionizing event. The drift time of these ions from the collision site to the cathode will depend on the mass and the position of the ionizing events. Recording the drift time of the ion and its hit position on the cathode provide a 3D image of the beam trajectory.

Fig. 2. Part a shows the position signals at the cathode depicting the trajectory of the beam, part (b) shows the vertical drift time, typically a few hundred ns long, for different ion species produced in collision of beam particle with the residual nitrogen gas. Part (c) shows the variation in sampling probability as a function of ambient gas pressure, which show perfect correlation over a span of three decades.

Fig. 3. The two most common geometries of beam monitors based on detection of secondary electron emissions, are shown in part (a) (linear geometry) and (b) (mirror geometry). The designs shown are generic and there are many different implementation of these detectors in which different position sensing devices are used to measure electron positions. Among these are MCPs backed by phosphors [8] and position sensitive multi-wire gas-filled detectors [9].

Fig. 4. The detector from Fig. 3a is shown here with the addition of two permanent magnets. The strength of the magnetic field near the foil determines the overall position

resolution that can be achieved. The ratio of magnetic field strength in front of the detector to that in front of the foil will determine the overall image magnification.

Fig. 5. Shows the image obtained with a detector set for large magnification and good position resolution. The two thin wires clearly visible at the detector image plane (left side) are images of wires with 0.1 mm and 0.25 mm diameter (shown at right).

Fig. 6. This figure shows the large aperture size spanned by a detector set up for a factor of  $\sim 3$  in image demagnification. The image of an 11 cm  $\times$  7 cm grid is projected on to a round 4-cm diameter position-sensitive MCP. Using larger MCP detectors and arranging them in a linear array can provide an even larger aperture for detection,

Fig. 7. Efficiency measurements of the two detectors are based on the premise that both detectors have the same efficiency and that any particle detected in the second detector (TD2) must have passed through the first detector (TD1) so any missing count in DT1 triggered by DT2 must be due to detector inefficiency.

Fig. 8. Shows a TAC spectrum obtained for 160 MeV  $^{17}\text{F}$  beam at 2-3 MHz counted by two detectors as outlined in Fig. 7. The large background is due to unavoidable random counts occurring during the 200 ns long counting period during which the TAC was open to accept any delayed stop signal from DT1. The counts in the second detector were scaled down by a factor of 1024 before triggering the TAC start signal,

Fig. 9. Data taken at the achromatic focus of the RMS to sample the isobar composition of beams used in reaction studies in the chamber in front of the RMS. The targets used are a few  $\text{mg}/\text{cm}^2$ , they are thick but allow the beam to pass. Coincidences with the MCP-based timing detector placed in front of the target allow for background suppression.

Fig 10. The beamline components used in a test of the isobar separation technique. The absorber, which is a specially designed gas cell filled with isobutane, is inserted close to the first timing detector. Residual energy, rather than energy loss is measured via time-of-flight technique, which allows for isobar tagging at a rate near  $10^6/\text{s}$ .

Fig. 11. Shows the predicted time-of-flight spectra for two  $A = 132$  isobars (a). The simulation for finite object size, includes effect of detector timing resolution, non-isochronous particle trajectories in the beamline, charge-state distribution and straggling of the ions after the absorber. Part b shows the data taken with  $A = 132$  isobars accelerated at HRIBF to 450 MeV.

Fig 12. The predicted time-of-flight spectrum for a beam mixture at 40 MeV that contained a 10:1 ratio of  $^{17}\text{O}:^{17}\text{F}$  mixture. The energy loss needed to achieve this level of separation is near 20 MeV; smaller energy loss near 5 MeV would probably be sufficient to get good separation.

Fig. 13. The electronic phosphor display. The beamline with two timing detectors followed by a movable four-jaw slit and the position-sensitive detector downstream are shown at the top of the figure. At the bottom are two composite display snapshots showing the phosphor display when slits are wide open and partly closed. The horizontal strips seen at the bottom of each panel are sliding bars updating displays that indicate the count rate in the two beam counters and the position-sensitive detector. These visual scalers proved to be very useful when searching for beam that is almost non-existent at the start.

**Table 1.** List of diagnostic methods/devices used with low-intensity beams. The notes provide some additional information and references to articles that describe the use of these devices with low-intensity and radioactive beams.

<b>Device</b>	<b>Performance Intensity range</b>	<b>Performance Energy range</b>	<b>Function</b>	<b>Notes</b>
Phosphor + Camera.	$10^4 - 10^{10}$	$>1\text{MeV}$	Profile	1
Moving wire w/amplification.	$10^7 - 10^{10}$	$>100\text{keV}$	Profile, sample Count,	2
Scintillators	$10^0 - 10^{10}$	$>1\text{MeV}$	profile Count,	3
Scintillating fibers	$10^0 - 10^7$	$>10\text{ MeV/A}$	profile	4
Gas (and other) detectors.	$10^0 - 10^5$	$>1\text{MeV}$	Count, profile	5
Residual gas ionization	$10^4 - 10^{13}$	$>100\text{ keV}$	Count, sample	6
Secondary electron emission.	$10^0 - 10^7$	$>100\text{ keV}$	Count, profile	7

# 3-D Beam Profile Sampling

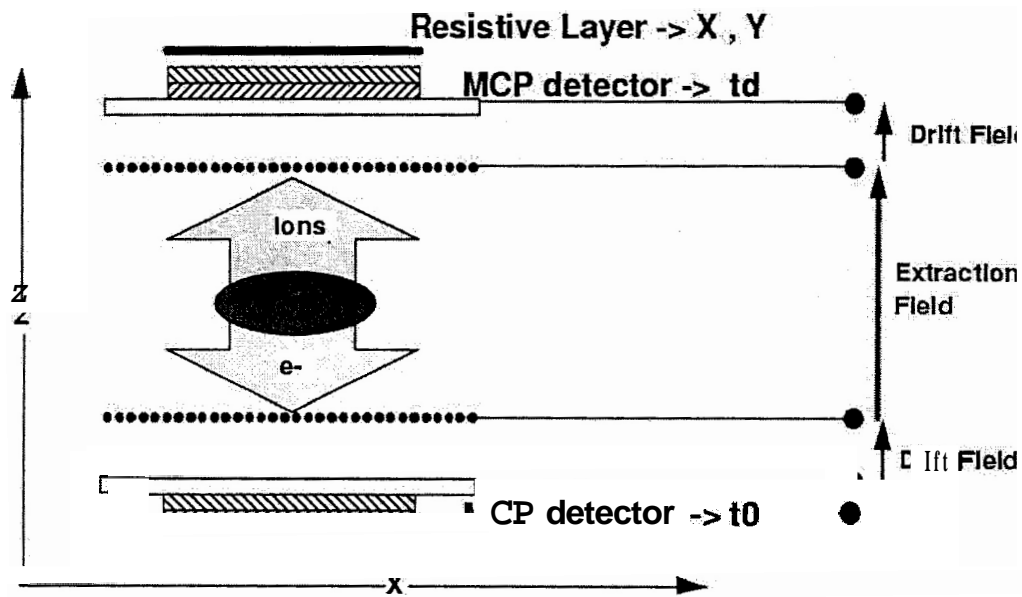


Fig. 1. The ions transported from the position where ionization of the residual gas molecule occurred retain information on the position of the ionizing event. The drift time of these ions from the collision site to the cathode will depend on the mass and the position of the ionizing events. Recording the drift time of the ion and its hit position on the cathode provide a 3D image of the beam trajectory.

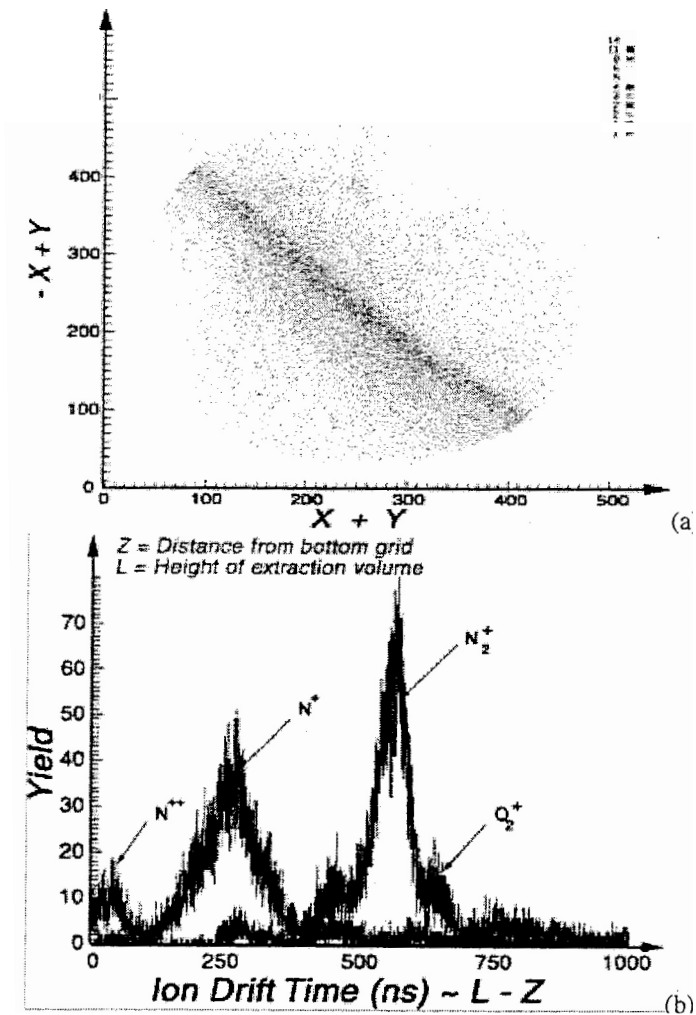


Fig. 2. Part (a) shows the position signals at the cathode depicting the trajectory of the beam, part (b) shows the vertical drift time, typically a few hundred ns long, for different ion species produced in collision of beam particle with the residual nitrogen gas. Part (c) shows the variation in sampling probability as a function of ambient gas pressure, which show perfect correlation over a span of three decades.

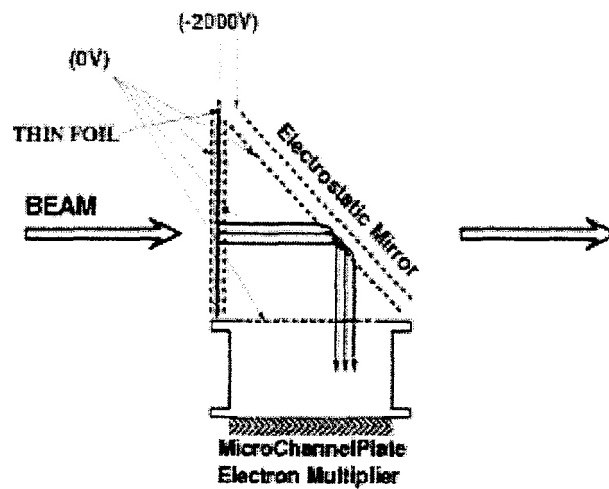
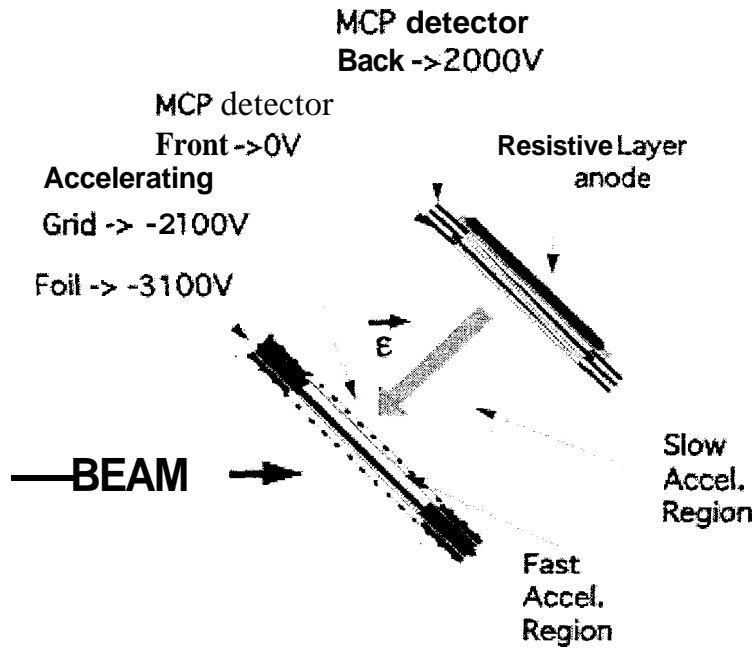


Fig. 3. The two most common geometries of beam monitors based on detection of secondary electron emissions, are shown in part (a) (linear geometry) and (b) (mirror geometry). The designs shown are generic and there are many different implementations of these detectors in which different position sensing devices are used to measure electron positions. Among these are MCPs backed by phosphors [8] and position sensitive multi-wire gas-filled detectors [9].

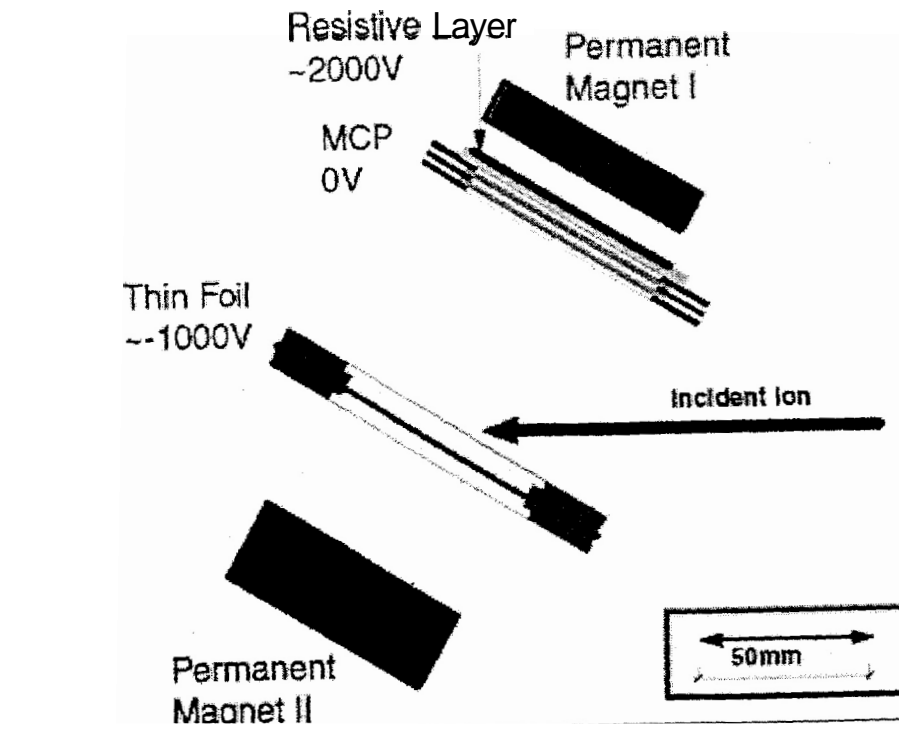


Fig. 4. The detector from Fig. 3a is shown here with the addition of two permanent magnets. The strength of the magnetic field near the foil determines the overall position resolution that can be achieved. The ratio of magnetic field strength in front of the detector to that in front of the foil will determine the overall image magnification.

Image of a 2mm wide strip, a 0.25mm wire and a 0.1 mm wire  
Image Magnification x3

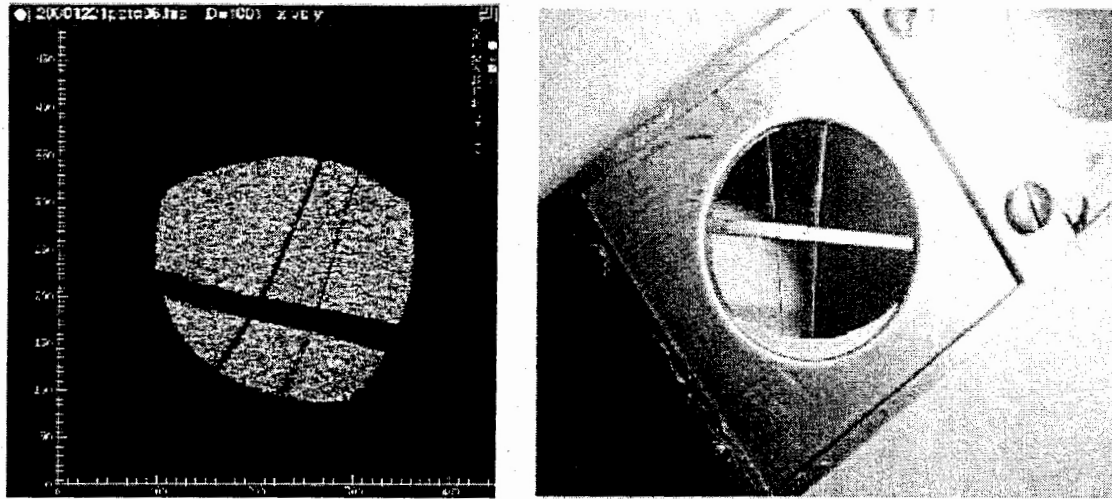
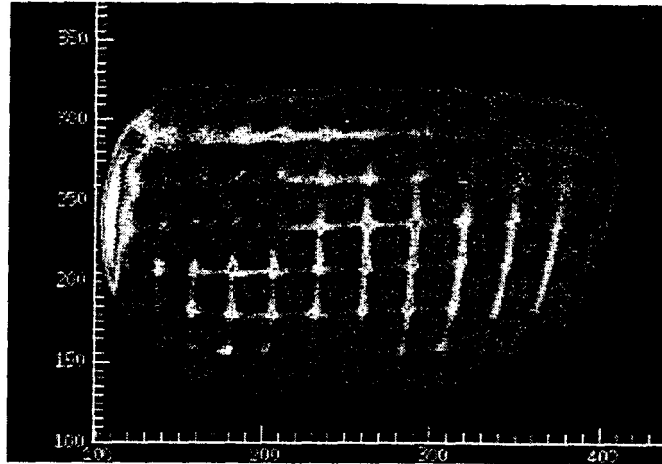
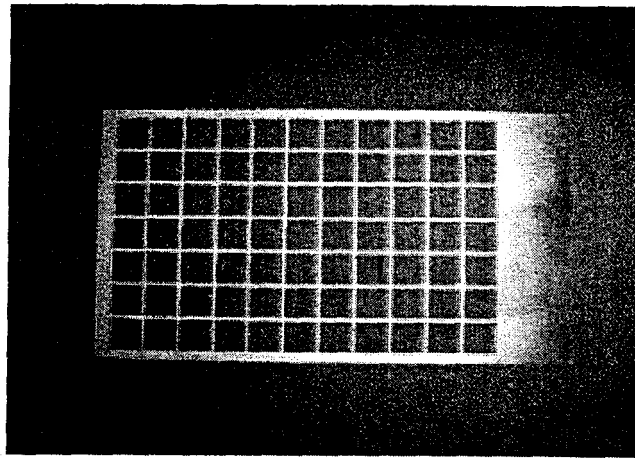


Fig. 5. Shows the image obtained with a detector set for large magnification and good position resolution. The two thin wires clearly visible at the detector image plane (left side) are images of wires with 0.1 mm and 0.25 mm diameter (shown at right).



(a)



(b)

Fig. 6. This figure shows the large aperture size spanned by a detector set up for a factor  $-3$  in image demagnification. The image of an  $11\text{ cm} \times 7\text{ cm}$  grid is projected on to a round  $4\text{-cm}$  diameter position-sensitive MCP. Using larger MCP detectors and arranging them in a linear array can provide an even larger aperture for detection.

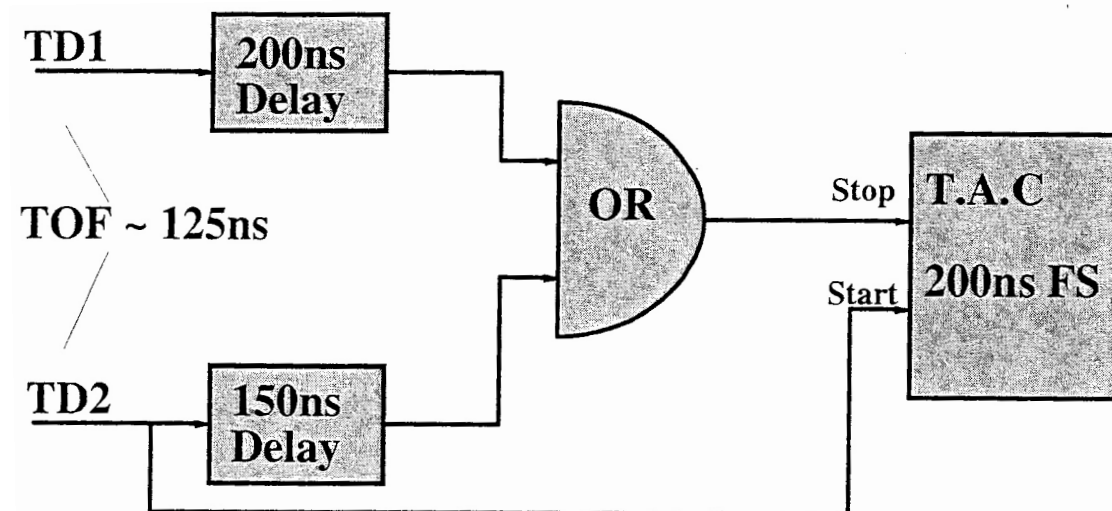


Fig. 7. Efficiency measurements of the two detectors are based on the premise that both detectors have the same efficiency and that any particle detected in the second detector (TD2) must have passed through the first detector (TD1) so any missing count in DT1 triggered by DT2 must be due to detector inefficiency.

## TOF spectrum (DT1-DT2)

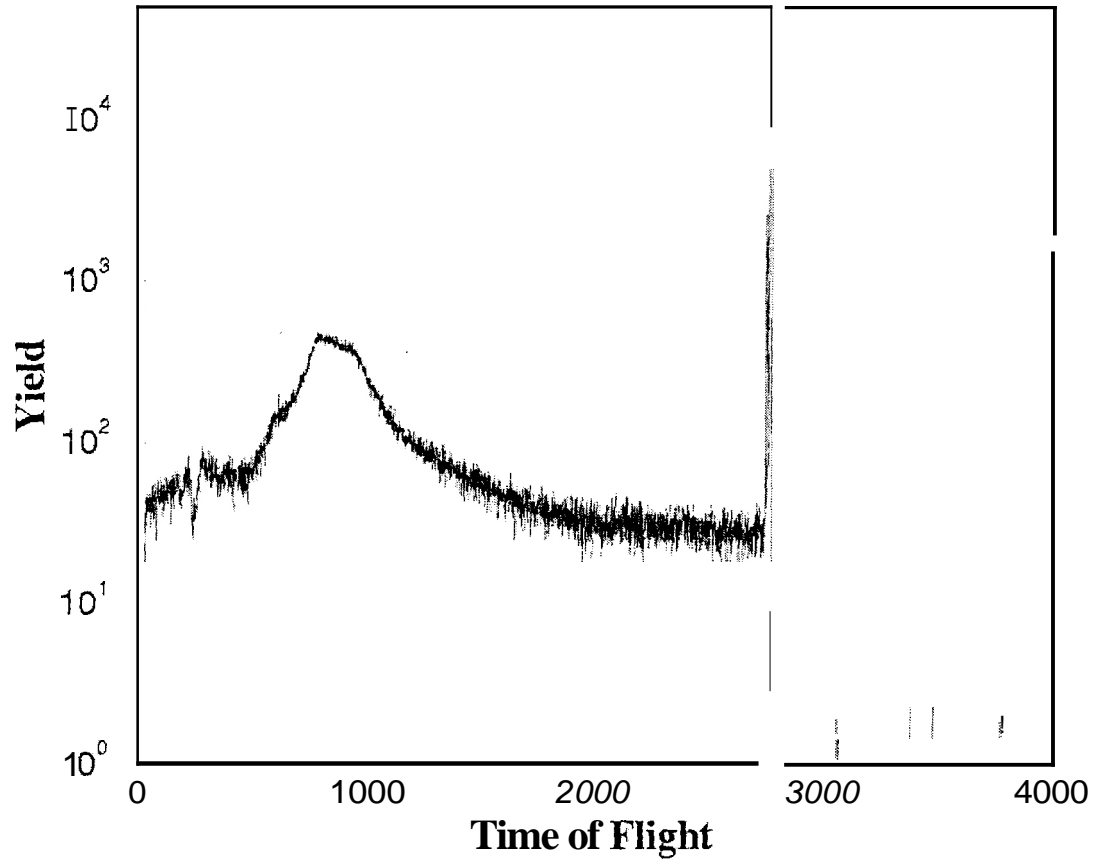


Fig. 8. Shows a TAC spectrum obtained for 160 MeV  $^{17}\text{F}$  beam at 2-3 MHz counted by two detectors as outlined in Fig. 7. The large background is due to unavoidable random counts occurring during the 200 ns long counting period during which the TAC was open to accept any delayed stop signal from DT1. The counts in the second detector were scaled down by a factor of 1024 before triggering the TAC start signal.

## Beam Composition from X-rays

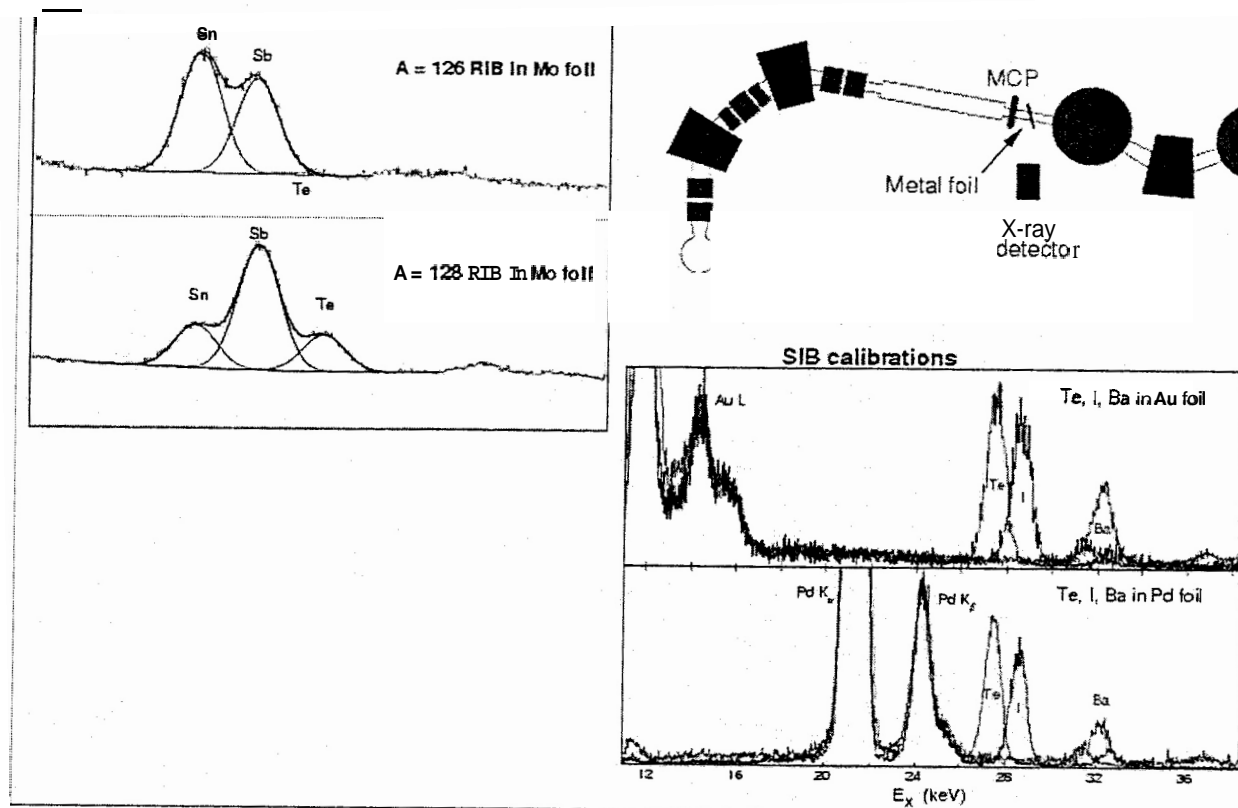


Fig. 9. Data taken at the achromatic focus of the Recoil Mass spectrometer (RMS) to sample the isobar composition of beams used in reaction studies in the chamber in front of the RMS. The targets used are a few  $\text{mg}/\text{cm}^2$ ; they are thick but allow the beam to pass. Coincidences with the MCP-based timing detector placed in front of the target allow for background suppression.

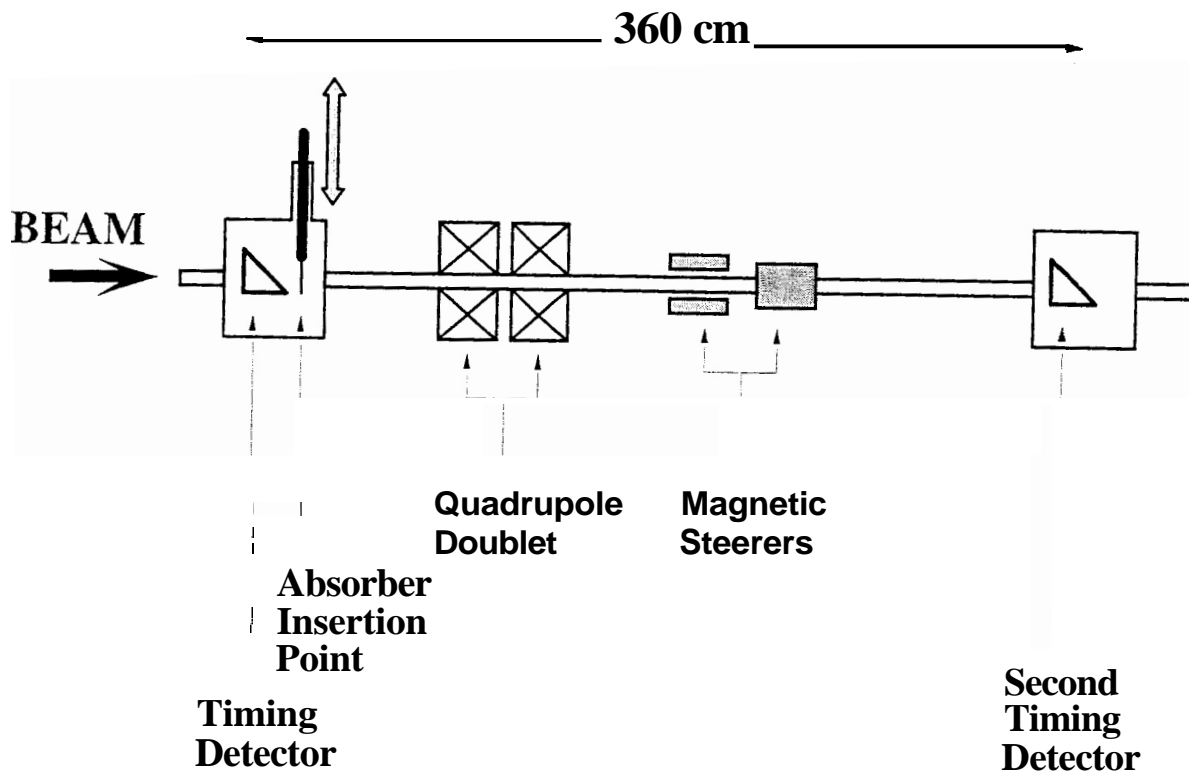


Fig 10. The beamline components used in a test of the isobar separation technique. The absorber, which is a specially designed gas cell filled with isobutane, is inserted close to the first timing detector. Residual energy, rather than energy loss is measured via time-of-flight technique, which allows for isobar tagging at a rate near  $10^6/s$ .

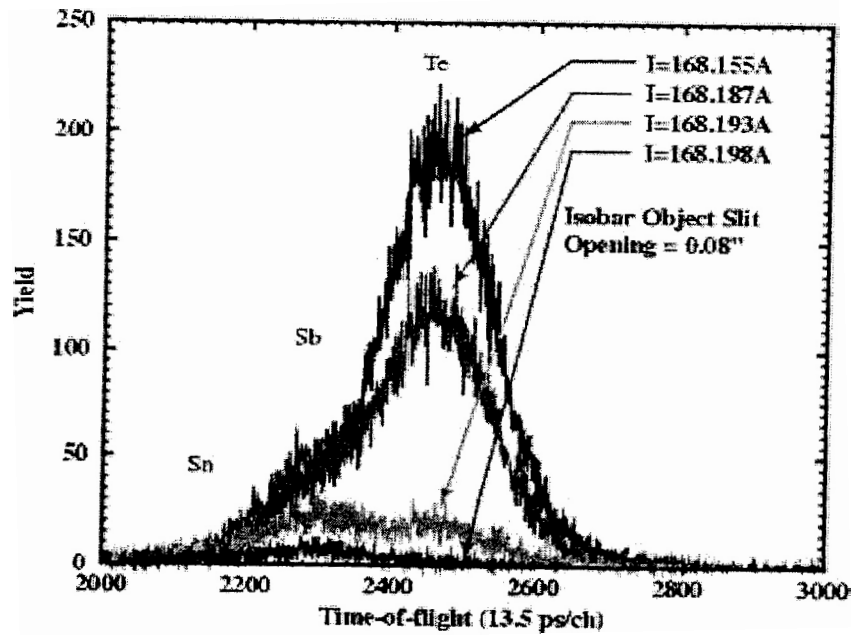
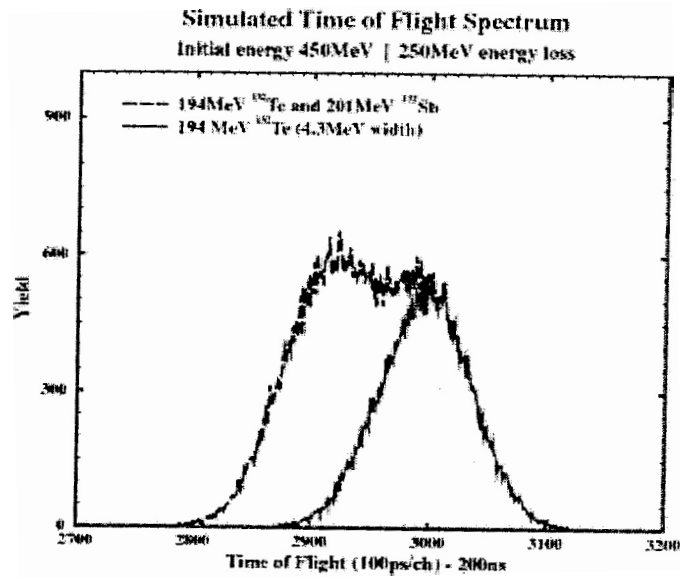


Fig. 11. Shows the predicted time-of-flight spectra for two  $A = 132$  isobars (a). The simulation for finite object size includes effect of detector timing resolution, non-isochronous particle trajectories in the beamline, charge-state distribution and straggling of the ions after the absorber. Part (b) shows the data taken with  $A = 132$  isobars accelerated at HRIBF to 450 MeV.

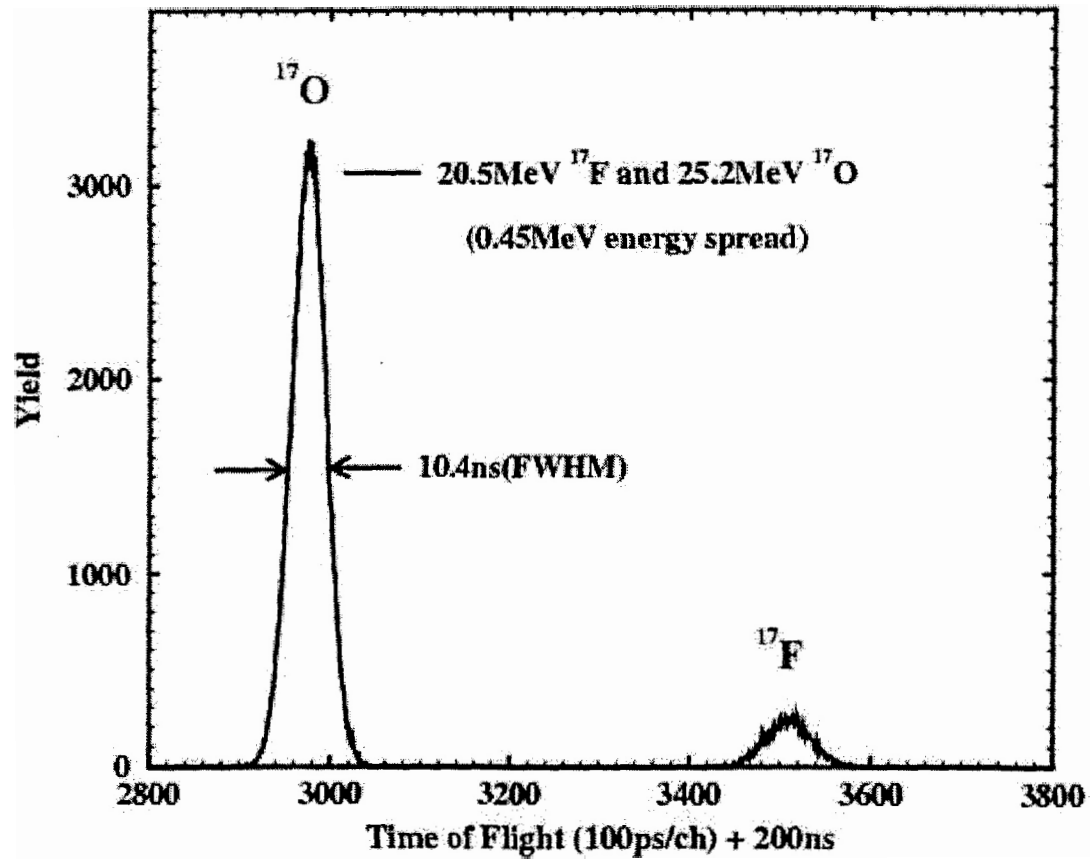
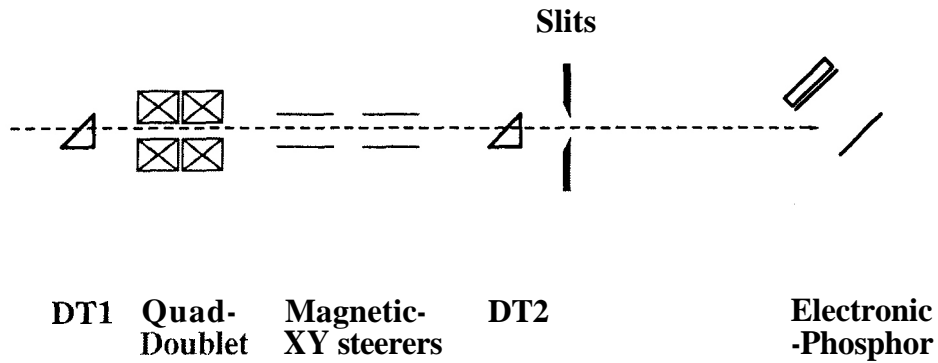


Fig 12. The predicted time-of-flight spectrum for a beam mixture at 40 MeV that contained a 10:1 ratio of  $^{17}\text{O}$ : $^{17}\text{F}$  mixture. The energy loss needed to achieve this level of separation is near 20 MeV; smaller energy loss near 5 MeV would probably be sufficient to get good separation.



"Real time" display of electronic phosphor  
and beam line detector rates (DT1 & DT2)

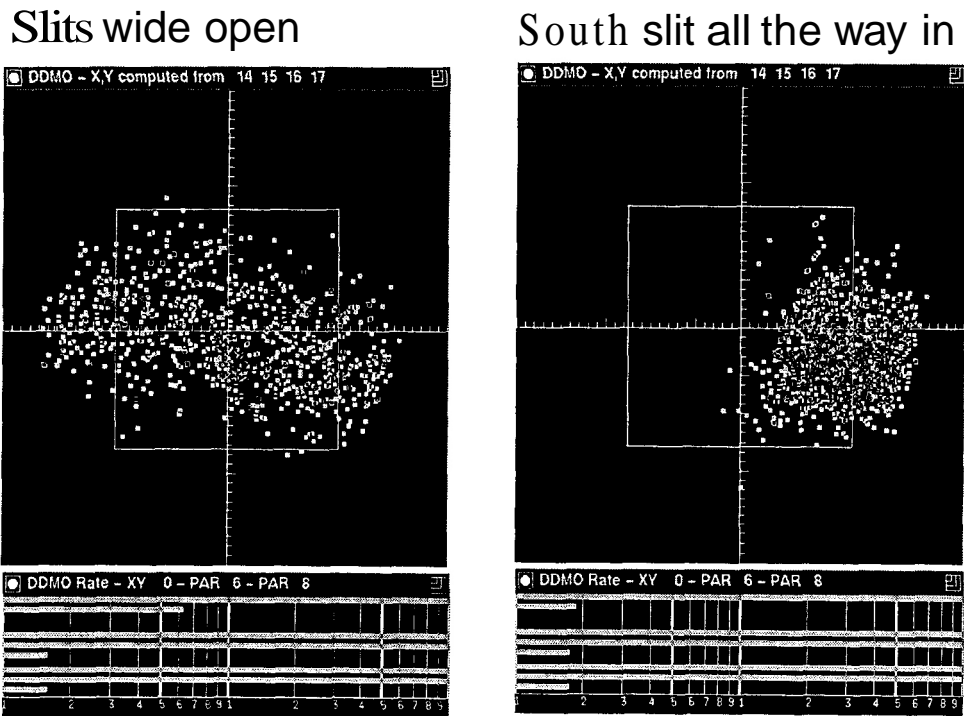


Fig. 13. The electronic phosphor display. The beamline with two timing detectors followed by a movable four-jaw slit and the position-sensitive detector downstream are shown at the top of the figure. At the bottom are two composite display snapshots showing the phosphor display when slits are wide open and partly closed. The horizontal strips seen at the bottom of each panel are sliding bars updating displays that indicate the count rate in the two beam counters and the position-sensitive detector. These visual scalars proved to be very useful when searching for beam that is almost non-existent at the start.